JOURNAL OF PROPULSION AND POWER
Vol. 16, No. 2, March–April 2000

Direct Computation of Jet Noise Produced by Large-Scale Axisymmetric Structures

R. R. Mankbadi,* S. H. Shih,† R. Hixon,† and L. A. Povinelli‡
John H. Glenn Research Center at Lewis Field, Cleveland, Ohio 44135

A methodology is presented for directly calculating the noise emission associated with large-scale structures in a supersonic jet. The nonlinear governing equations are solved in a computational domain that encompasses both the jet flow and the acoustic near field. A high-order discretization scheme is used along with careful boundary treatment to capture the disturbance field accurately. Nonlinear interactions among the various frequency modes of the flow structure were found to alter the development of each mode and, hence, influence its radiation pattern. Comparing the calculated radiation pattern to experimental observations indicates that the axisymmetric structure contributes preferentially in the forward direction, whereas the azimuthal structure is associated with a higher emission angle and with a stronger effect on jet spreading. Sensitivity of the radiated sound field to the type of incoming disturbances is studied.

Nomenclature

D	= nozzle diameter
E	= total energy
F, G, H	= fluxes in the x, r, and ϕ directions, respectively
I	= enthalpy
M	= Mach number
p	= pressure
$\boldsymbol{Q}$	= unknown dependent variables
T	= temperature
u, v, w	= velocities in the x, r, and ϕ directions
x, r, ϕ	= cylindrical coordinates
Δ	= mesh spacing
ν	= effective viscosity
ρ	= density
σ	= viscous stresses
τ	= unresolved stresses

I. Introduction

SEVERAL recent attempts have been made to calculate jet noise by solving the time-dependent governing equations to obtain the flow fluctuations and then to use some other technique to obtain the corresponding radiation field. Unsteady jet flow can be calculated with various degrees of approximation using large-eddy simulations,[1–5] a nonlinear integral approach,[6] linearized Euler equations,[7] or linear stability equations.[8,9] The corresponding sound field can be calculated using acoustic analogy,[10] surface integral methods,[11,12] linearized Euler equations,[13] or asymptotic methods.[8,9] For further details the reader is referred to reviews in Refs. 14 and 15.

In the direct approach, the computational domain encompasses both the flow and the acoustic disturbance fields. Direct Numerical Simulations (DNS) using the full, time-dependent compressible Navier–Stokes equations can completely describe the process of sound generation and propagation. However, the resolution requirements for high Reynolds number turbulent flows make DNS impractical due to current computer capabilities. Alternatively, one may focus on understanding the individual mechanisms involved to develop technologies for faster computation of jet noise or for control of the dominant mechanisms. Tam et al.[16] have attempted to classify the jet noise resulting from the mixing of the flow fluctuations into two contributions: one attributed to large turbulence structure and the other attributed to fine-scale turbulence. It is believed that the smaller scales are less efficient than the larger scales in radiating sound.[17–20] There is no clear distinction between the two sources. We compute herein the noise attributed to the large-scale structure, which is taken to be that produced by the numerically resolved structure.

In the present approach the acoustically relevant, large-wavelength scales are resolved. As with large-eddy simulations (LES), the effects of the unresolved scales on those that are resolved are accounted for. The wave number range of the acoustically relevant scales may be smaller than that usually resolved in conventional LES. For this reason, we prefer to label the present approach large-scale simulations (LSS) rather than LES. In Ref. 7 LES were presented with emphasis on capturing the sound source as given by the jet flow fluctuations. In the present LSS, the computational domain is extended, and the boundary treatment is modified to capture both the flow oscillations and the radiated sound directly.

We present in Sec. II the large-scale nonlinear equations governing the flow and acoustic fields of a round jet. These equations are obtained by filtering the full Navier–Stokes equation and by modeling the effect of the unresolved scales on the resolved ones. A high-order numerical scheme and careful boundary treatments are needed, otherwise the computed solution will be contaminated, and the physical flow and acoustic disturbances cannot be accurately captured. These issues will be discussed in Secs. III and IV. Results for the effect of the magnitude and spectrum of the inflow disturbances on the jet noise will be presented in Sec. V followed by conclusions in Sec. VI.

II. Governing Equations

The problem under consideration is that of a supersonic jet issuing from a nozzle of diameter D. The full compressible Navier–Stokes equations describe both the flow and acoustic fluctuations. A spatial filter is introduced in the form

$$f(x) = \int K(x - \xi, \Delta) f(\xi)\, \mathrm{d}\xi \tag{1}$$

where K is the spatial filter function, Δ is the computational mesh size. Upon applying this filter to the flow variables, the flowfield can be decomposed into

$$f = \bar{f} + f'' \tag{2}$$

Presented as Paper 95-0680 at the 33rd Aerospace Sciences Meeting and Exhibit, 9–12 January 1995, Reno, NV; received 17 July 1998; revision received 31 March 1999; accepted for publication 1 April 1999.

*Technical Leader, CAA, ICOMP; fsmankb@lerc.nasa.gov. Associate Fellow AIAA.
†Senior Research Associate. Member AIAA.
‡Chief Scientist, Turbomachinery Division. Fellow AIAA.

where an overbar denotes the resolved (filtered) field and a prime denotes the unresolved (subgrid) field. The mean of the filtered field is the mean of the total field. Upon substituting this splitting into the full Navier–Stokes equation, the filtered compressible Navier–Stokes equation takes the form (Ref. 21, Chapter 9)

$$\frac{\partial \boldsymbol{Q}}{\partial t} + \frac{\partial F}{\partial x} + \frac{1}{r}\frac{\partial G}{\partial r} + \frac{\partial H}{r\partial \phi} = S \tag{3}$$

$$\boldsymbol{Q} = [\bar{\rho}, \bar{\rho}\tilde{u}, \bar{\rho}\tilde{v}, \bar{\rho}\tilde{w}, \bar{\rho}\tilde{e}]^T \tag{4}$$

$$F = \begin{bmatrix} \bar{\rho}\tilde{u} \\ \bar{p} + \bar{\rho}\tilde{u}^2 - \tilde{\sigma}_{xx} - \tau_{xx} \\ \bar{\rho}\tilde{u}\tilde{v} - \tilde{\sigma}_{xr} - \tau_{xr} \\ \bar{\rho}\tilde{u}\tilde{w} - \tilde{\sigma}_{x\phi} - \tau_{x\phi} \\ \bar{\rho}\tilde{u}\tilde{I} - \tilde{u}\tilde{\sigma}_{xx} - \tilde{v}\tilde{\sigma}_{xr} - \tilde{w}\tilde{\sigma}_{r\phi} - \tilde{K}\dfrac{\tilde{\partial}T}{\partial x} - c_v q \end{bmatrix} \tag{5}$$

$$G = \begin{bmatrix} \bar{\rho}\tilde{v} \\ \bar{\rho}\tilde{u}\tilde{v} - \tilde{\sigma}_{xr} - \tau_{xr} \\ \bar{p} + \bar{\rho}\tilde{v}^2 - \tilde{\sigma}_{rr} - \tau_{rr} \\ \bar{\rho}\tilde{v}\tilde{w} - \tilde{\sigma}_{r\phi} - \tau_{r\phi} \\ \bar{\rho}\tilde{v}\tilde{I} - \tilde{u}\tilde{\sigma}_{xr} - \tilde{v}\tilde{\sigma}_{rr} - \tilde{w}\tilde{\sigma}_{r\phi} - \tilde{K}\dfrac{\partial \tilde{T}}{\partial r} - c_v q \end{bmatrix} \tag{6}$$

$$H = \begin{bmatrix} \bar{\rho}\tilde{w} \\ \bar{\rho}\tilde{u}\tilde{w} - \tilde{\sigma}_{x\phi} - \tau_{x\phi} \\ \bar{\rho}\tilde{v}\tilde{w} - \sigma_{r\phi} - \tau_{r\phi} \\ \bar{p} + \bar{\rho}\tilde{w}^2 - \tilde{\sigma}_{\phi\phi} - \tau_{\phi\phi} \\ \bar{\rho}\tilde{w}\tilde{I} - \tilde{u}\tilde{\sigma}_{x\phi} - \tilde{v}\tilde{\sigma}_{r\phi} - \tilde{w}\tilde{\sigma}_{\phi\phi} - \tilde{K}\dfrac{\partial \tilde{T}}{\partial \phi} - c_v q \end{bmatrix} \tag{7}$$

$$S = \begin{bmatrix} 0 \\ 0 \\ \tilde{p} + \tilde{p}\tilde{w}^2 - \tilde{\sigma}_{\phi\phi} - \tau_{\phi\phi} \\ -\tilde{v}\tilde{w} - \tilde{\sigma}_{r\phi} - \tau_{r\phi} \\ 0 \end{bmatrix} \tag{8}$$

where $\boldsymbol{Q}$ is the unknown vector and F, G, and H are the fluxes in the axial direction x, the radial direction r, and the azimuthal direction ϕ, respectively. S is the source term that arises in cylindrical polar coordinates, κ is thermal conductivity, e is the internal energy, and σ_{ij} are the viscous stresses. This system of equations is coupled with the equation of state for a perfect gas. Here, a tilde denotes Favre averaging:

$$\tilde{f} = \overline{\rho f}/\bar{\rho} \tag{9}$$

Velocities are normalized by the streamwise velocity at the jet exit centerline, density is normalized by the exit centerline density, and distances are normalized by the nozzle radius $D/2$.

The unresolved stresses τ_{ij} appearing in Eqs. (5–8) need to be modeled. The objective herein is to capture a certain range of acoustically efficient scales. Thus, the unresolved scales may be different from those of conventional LES, and an appropriate subgrid scale model is needed. Because such a model is lacking at present, a compressible version of Smagornisky's model[22] is used to establish the basic concept. Implementing such a model increases the dissipation, which in some cases smooths out abrupt changes. In Smagornisky's model, the subgrid-turbulence stresses are modeled as

$$\tau_{ij} = k_g \delta_{ij}/3 - 2\rho\nu_R\left(\tilde{S}_{ij} - \tfrac{1}{3}\delta_{ij}\tilde{S}_{mm}\right) \tag{10}$$

where k_g is the kinetic energy of the residual turbulence. The strain rate of the resolved scale is given by

$$\tilde{S}_{ij} = \frac{1}{2}\left(\frac{\partial \tilde{u}_i}{\partial x_j} + \frac{\partial \tilde{u}_j}{\partial x_i}\right) \tag{11}$$

The summation $\tilde{S}_{mm}$ is zero for incompressible flow, ν_R is the effective viscosity of the residual field,

$$\nu_R = (C_s \Delta_f)^2 \sqrt{2 S_{mn} S_{mn}} \tag{12}$$

and Δ_f is the filter width given by

$$\Delta_f = (\Delta_x \Delta_y \Delta_z)^{\frac{1}{3}} \tag{13}$$

For the heat equation, the eddy viscosity is modeled as[23]

$$q = \bar{\rho}\frac{\nu_t}{Pr_t}\frac{\partial \tilde{T}}{\partial x_k} \tag{14}$$

where Pr_t is the subgrid-scale turbulent Prandtl number, which can be taken as 0.5, and $C_s = 0.23$ (Ref. 24).

III. Discretization of the Governing Equations

A high-order discretization scheme is required to capture the wavelike disturbances with a minimum of dispersion and dissipation errors. A fourth-order space-accurate, second-order time-accurate MacCormack-type scheme[25,26] is used. The operator is split into one-dimensional operators, which for the two-dimensional case takes the form

$$Q^{n+2} = L_{x1} L_{r1} L_{r2} L_{x2} Q^n \tag{15}$$

Each operator consists of a predictor step and a corrector step using one-sided differencing as follows.

Predictor:

$$Q_i^{n+\frac{1}{2}} = Q_i^n - \frac{\Delta t}{6\Delta x}(7F_i - 8F_{i-1} + F_{i-2})^n \tag{16}$$

Corrector:

$$Q_i^{n+1} = \frac{1}{2}\left(Q_i^{n+\frac{1}{2}} + Q_i^n + \frac{\Delta t}{6\Delta x}(7F_i - 8F_{i+1} + F_{i+2})^{n+\frac{1}{2}}\right) \tag{17}$$

and likewise for the other directions. The sweep directions are reversed between operators to avoid biasing. Flux quantities outside of the computational boundaries are obtained via third-order extrapolation of the interior quantities when needed.

IV. Boundary Treatments

The computation domain is finite, and numerical boundary treatments need to be applied at the boundaries to depict the appropriate physics. This, particularly for high-order finite difference schemes, could generate spurious modes that render the computed solution entirely useless. Several boundary treatments need to be applied at the computation boundary, as shown in Fig. 1. At $x = x_{\min}$, the nozzle exit flow spans $0 < r < D/2$, this is followed in the radial direction by an entertainment regime and then a radiation regime. At $r = r_{\max}$, the radiation condition applies along x. At $x = x_{\max}$, an outflow condition is applied from $r = 0$ to the radial location, where the radiation condition applies. For each of these domains the appropriate boundary treatment needs to be applied. Several suggestions for boundary conditions that might be suitable for computational aeroacoustics have recently been proposed and have been reviewed in Refs. 27 and 28. The following treatments were found to produce a stable solution nearly free from reflections.

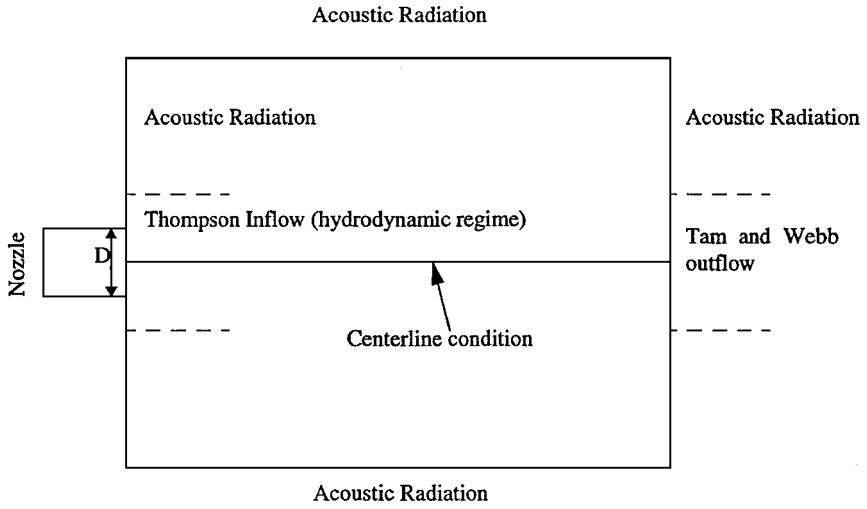

Fig. 1 Computational domain.

A. Inflow Boundary

In real jets, the engine flow determines the disturbance incoming to the jet plume.[29] Furthermore, the generated noise could feed back and influence the disturbances through the engine intake and through the nozzle-lip shear-layer receptivity. A full simulation including the engine is not currently feasible; as such, the problem needs to be simplified. In the following, the computation domain starts at the nozzle exit, where the nozzle exit flow is supersonic and the inflow disturbances to the jet plume are specified. Outside the nozzle, the flow gradually switches to subsonic and diminishes. For $r/D > 2$, the acoustic radiation condition is applied. For $r/D < 2$, the inflow is characterized by supersonic and subsonic regimes. In the supersonic regime, all characteristics travel in the flow direction. The primitive variables given at $x = x_{\min}$ are taken as specified according to the type of inflow disturbance (Sec. V). In the subsonic regime, Thompson's[30] nonreflecting boundary condition is used. The following three characteristics, C_1, C_2, and C_3, are specified according to the inflow disturbances as

$$P_t + \rho c u_t = C_1, \qquad P_t - c^2 \rho = C_2, \qquad \rho c v_t = C_3 \tag{18}$$

The fourth characteristic, C_4, is outgoing and is obtained from the interior solution with a nonreflecting condition by rearranging the equations as

$$P_t - \rho c u_t = C_{4x} + C_{4r} \tag{19}$$

Where subscripts x and r denote the axial and radial derivative, respectively. C_{4x} is set to zero for a nonreflecting boundary condition. The four characteristics are then solved together to obtain the time derivative of the variables to update the solution at the inflow boundary. This allows feedback to affect the inflow disturbances at the subsonic regime.

B. Radiation Boundary Condition

The radiation condition is applied at $x = x_{\min}$, for $r/D > 2$, and at the lateral boundary, $r = r_{\max}$, $< 0 < x < x_{\max}$. Also, part of the outflow boundary, $x = x_{\max}$, where the Mach number is less than 0.01, is considered a radiation regime. The conventional acoustic radiation condition based on the asymptotic analysis of the wave equation is used, namely,

$$\{u_t, v_t, p_t, \rho_t\} = -\mho\left(\frac{\partial}{\partial R} + \frac{1}{R}\right)\{u, v, p, \rho\} \tag{20}$$

where

$$\mho = c_0\left\{(x/R)M + [1 - (r^2/R^2)M^2]^{\frac{1}{2}}\right\} \tag{21}$$

and

$$R = \sqrt{x^2 + r^2} \tag{22}$$

where M is the local Mach number and c_0 is the speed of sound. Spatial derivatives are obtained based on the interior solution.

C. Outflow Boundary Treatment

The asymptotic analysis of the convective wave equation[31,32] leads to

$$\frac{1}{\mho}\frac{\partial p'}{\partial t} + \frac{\partial p'}{\partial R} + \frac{p'}{R} = 0 \tag{23}$$

However, Tam and Webb's[33] asymptotic analysis shows that the governing equations support vorticity and density waves in addition to the acoustic waves, but that only the acoustic waves have a pressure component. To account for the presence of flow disturbances at the outflow, the momentum equations are solved to update the density and velocity components using one-sided differencing. The pressure equation (energy) is replaced by its asymptotic form to ensure outgoing waves. This condition is applied at $x = x_{\max}$ for the radial direction, where the exit Mach number is greater than 0.01.

D. Centerline Boundary

The results presented for axisymmetric disturbances and the boundary condition at $r = 0$ can be stated as

$$\frac{\partial}{\partial r}[u, p, \rho] = 0, \qquad v = 0 \tag{24}$$

This was implemented by setting the flux in the radial direction as $G = 0$. The centerline treatment for nonaxisymmetric disturbances is addressed in Refs. 34 and 35.

V. Results

The numerical results presented are for a perfectly expanded cold supersonic jet at a Mach number of 2.1. The total temperature of the jet is 294 K, and jet exit pressure is 0.0515 atm. The Reynolds number based on the jet exit conditions is approximately 7×10^4. The computational domain extends axially from $x/D = 2.5$ to 35 and radially from the centerline to $r/D = 16$, as shown in Fig. 1.

Three types of inflow disturbances are studied. In the first, a single-frequency disturbance corresponding to $St = 0.2$ is considered with nominal amplitude ϵ, which could vary between low and high initial levels. Here, $St = fD/U_e$, where f is the frequency in hertz and U_e is the jet exit velocity at the centerline. In the second type of inflow, the initial disturbances are composed of two

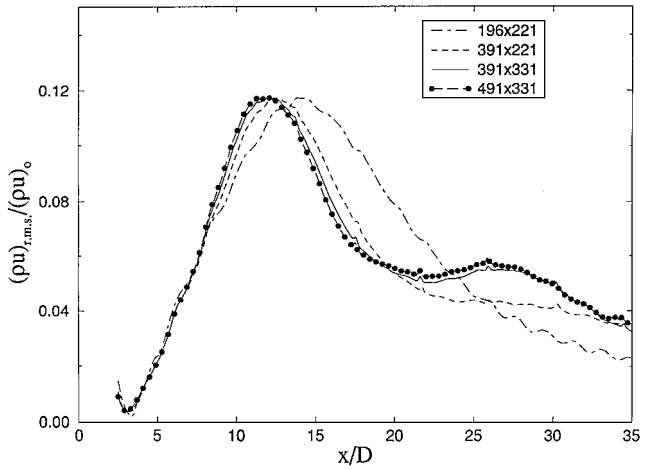

Fig. 2 Grid refinement study: development of the rms values of the axial momentum at $r/D = 0.5$.

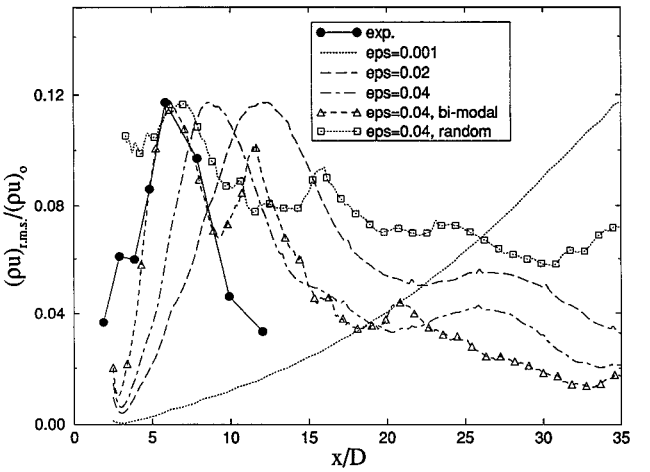

Fig. 3 Development of the rms values of axial momentum at $r/D = 0.5$ for various inflow disturbances.

frequencies corresponding to $St = 0.2$ and 0.4, with $\epsilon = 0.4$. In the third case, time-random inflow disturbances are considered. In the single- or two-frequency cases, the disturbances profiles are obtained by solving the Rayleigh equation describing the linear development of instability waves. The resulting eigenfunctions for the specified mean flow profile and frequency are taken to be the radial profiles of the disturbances. The initial mean flow profile used in solving the Rayleigh equation is that given in Ref. 36 to describe the experimental data of Troutt and McLaughlin. For the two-frequency case, an initial phase-difference angle β between the two is specified as $3\pi/2$ (Ref. 21, Chapter 6). For random-frequency excitation, the radial profiles of the disturbance are taken to be Gaussian, with an amplitude $A(t)$, which is a computer-generated random function. The random disturbances range is taken as $0.025 < St < 1.6$. The upper Strouhal number range is taken to avoid errors from inaccurate resolution of the higher frequencies, and the lower frequency range is set for spectral analysis of the data. A total of 32 random values is taken for each variable over uniform time steps from $t = 0$ to 40. An Akima spline is fitted through these points to determine the value of the input disturbances for each time level. The result is taken to be one period of the excitation, and at the end of each period, the excitation cycle is specified.

The grid points are equally spaced in the x direction. In the radial direction, the grid is stretched between the centerline and $r/D = 1$, with concentration around $r/D = 0.5$. Beyond $r/D = 1$, the geometric grid stretching is used until the radial spacing equals the axial spacing. Afterwards the grid is uniform in both directions. The numerical grid refinement study is conducted for the single-frequency excitation case at $St = 0.2$ at large amplitude corresponding to $\epsilon = 0.02$, wherein nonlinear effects are strong enough to generate various modes that fill the spectra. Four sets of grids are considered, 196 × 221, 391 × 221, 391 × 331, and 491 × 331, in the axial and radial directions, respectively. Figure 2 shows the streamwise development of the root-mean-square (rms) value of the axial momentum disturbance in the shear layer ($r/D = 0.5$). A grid-independent solution is obtained for the 391 × 331 or finer grids. Consequently, the 391 × 331 grid is used in the subsequent investigations.

A. Nonlinear Development of the Flow

In Figs. 3–5, we examine the nonlinear development of the flow disturbances under the various types of inflow excitation discussed earlier. The streamwise developments of the rms of the axial momentum disturbances are shown in Fig. 3. For the small input disturbances, the growth is exponential in accordance with the linear stability theory, and no saturation is reached within the computational domain. For high levels of input disturbance, the disturbances initially grow exponentially according to the linear stability theory, but as the disturbances continue to grow, nonlinear saturation is reached,

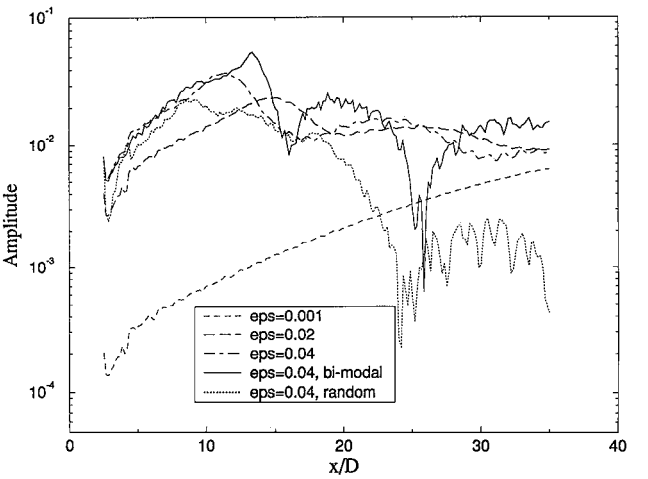

Fig. 4 Development of the amplitude of the pressure disturbance at $r/D = 0.5$.

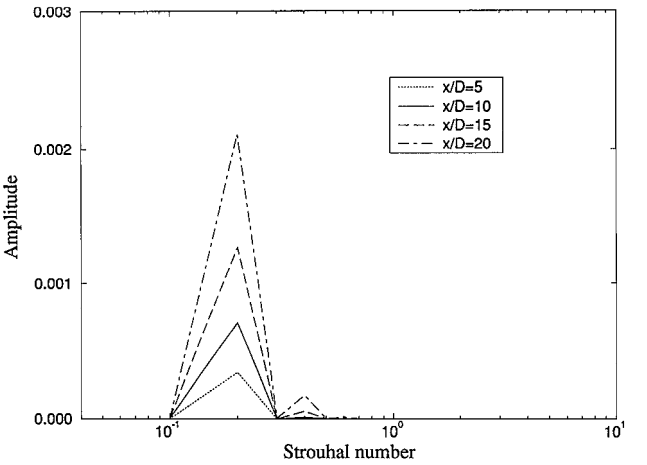

Fig. 5a Pressure spectra at $r/D = 0.5$, for single-frequency excitation, $\epsilon = 0.001$.

followed by slow decay. The nonlinear saturation mechanisms include self-interaction and fundamental–subharmonic interaction, as well as generation of and interaction with other sum and difference modes. Increasing the disturbance level or the number of modes causes nonlinear effects to come sooner, moving the location of the peak upstream. Additional peaks may appear downstream, which is typical of nonlinear interactions among the various disturbance modes for subsonic jets. The experimental results of Troutt and

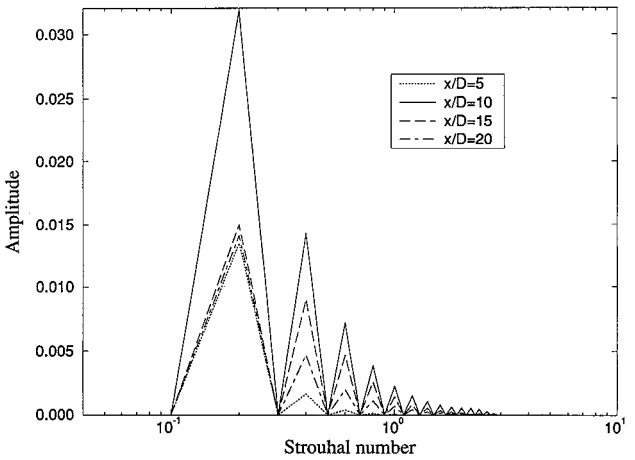

Fig. 5b Pressure spectra at $r/D = 0.5$, for single-frequency excitation, $\epsilon = 0.04$.

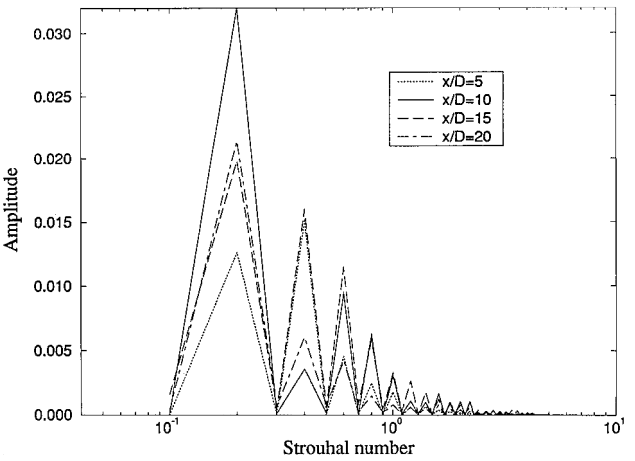

Fig. 5c Pressure spectra at $r/D = 0.5$, for two-frequency excitation, $\epsilon = 0.04$.

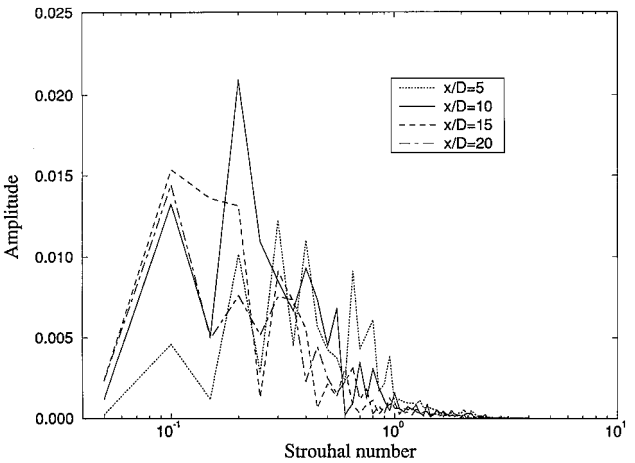

Fig. 5d Pressure spectra at $r/D = 0.5$, for random-frequency excitation, $\epsilon = 0.04$.

McLaughlin[36] are shown in Fig. 3 for comparison. The prediction qualitatively agrees with observations, but the decay rate is faster in the experiment due to the three-dimensional effects, which are absent in the present computation.

The amplitude of the pressure disturbance corresponding to $Sr = 0.2$ is shown in Fig. 4 for several types of inflow disturbances. For initially small amplitudes, the growth follows the linear stability theory. Comparing the $\epsilon = 0.04$ case of single-frequency excitation to that of bimodal excitation at the same level shows that the presence of the subharmonic reduces the peak of the fundamental ($Sr = 0.2$). For random inflow disturbances, the presence of several modes reduces the peak of the fundamental and increases its decay rate.

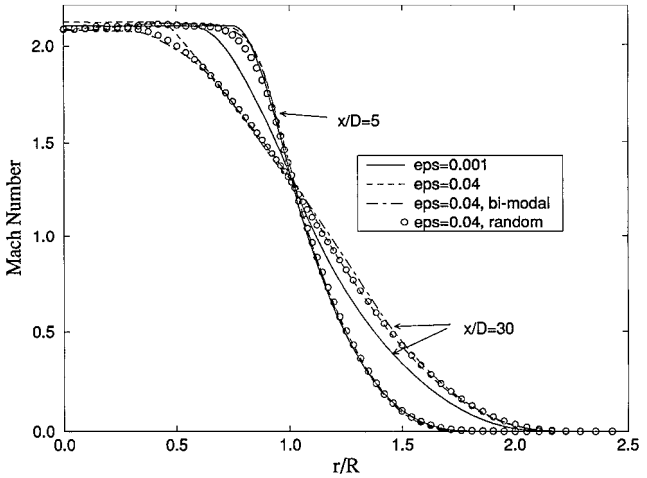

Fig. 6a Mean flow Mach number profiles at $x/D = 5$ and 30.

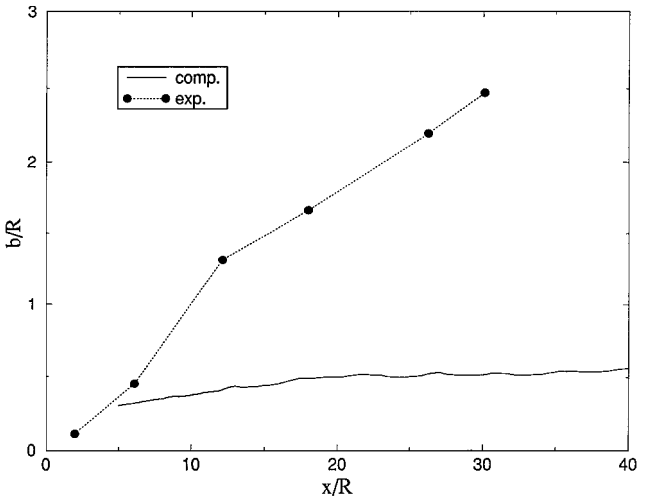

Fig. 6b Axial distribution of half-width of the shear layer, single-frequency excitation, $\epsilon = 0.04$.

The pressure spectra at $r/d = 0.5$ are shown in Fig. 5. In the low-disturbance case shown in Fig. 5a, there is practically no growth of frequency components, other than the input one, indicating linear behavior. In Fig. 5b, the spectra are shown for the case of single-frequency excitation, $\epsilon = 0.04$, where no harmonics were originally present. Figure 5b, however, shows considerable amplification of the harmonics due to the nonlinear wave–wave interaction. In the bimodal excitation case in Fig. 5c, the amplitude of the fundamental and subharmonic are initially comparable to each other, but they alternate dominance as they develop and interact downstream. In the random input case, there is initially no dominant frequency. However, as Fig. 5d indicates, a peak develops around $Sr = 0.25$ in accordance with the preferred Strouhal number concept for subsonic jets.[37]

Figure 6a shows the mean flow Mach number profiles at two streamwise locations. Higher excitation levels or more modes increase the spreading rate of the jet. The computed and measured half-width of the shear layer of the single-frequency excitation case is shown in Fig. 6b. The predicted spreading rate is lower than the experimental one. This is attributed to neglecting the three-dimensional structure, which for supersonic jets is more amplified than the axisymmetric one accounted for here.

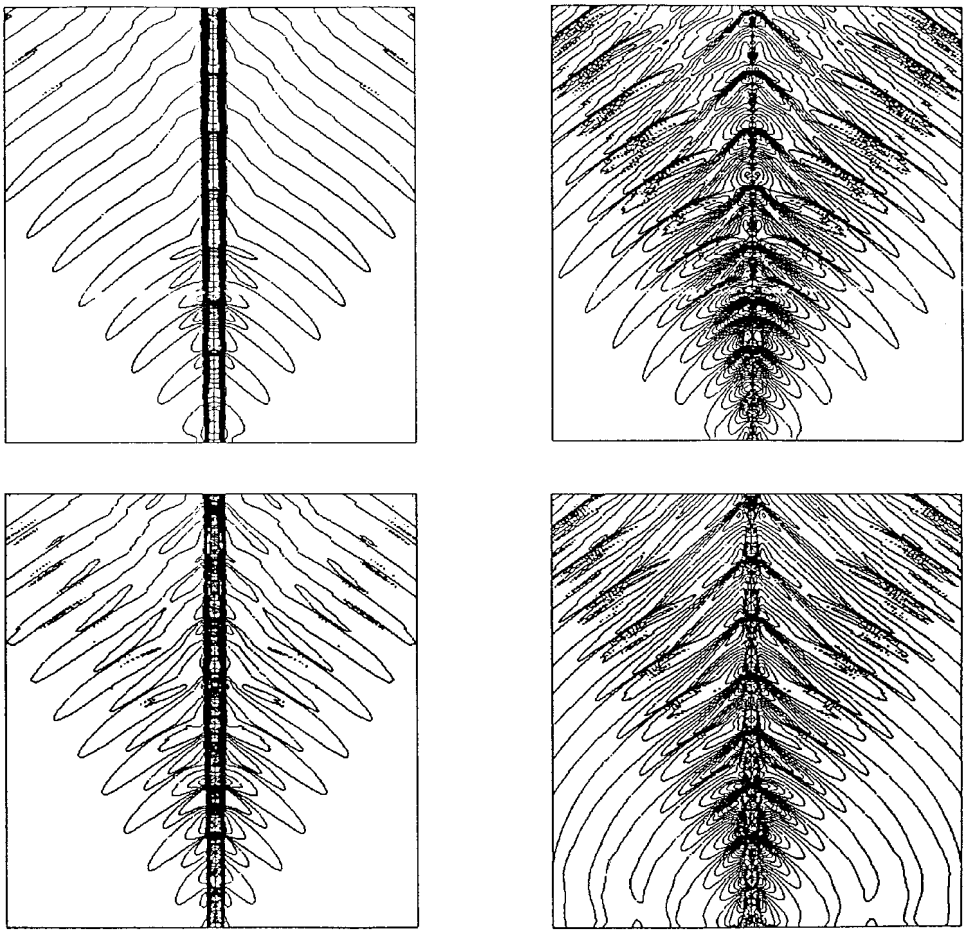

Fig. 7 Single frequency excitation at $\epsilon = 0.04$: a) density: $r_{min} = 0.5, r_{max} = 1.2$, and $\Delta\rho = 0.0175$; b) axial velocity: $u_{min} = 0.1, u_{max} = 1.2$, and $\Delta u = 0.0325$; c) radial velocity: $v_{min} = 0.06, v_{max} = 0.09$, and $\Delta v = 0.005$; and d) pressure: $p_{min} = 0.1, p_{max} = 0.2$, and $\Delta p = 0.0025$.

B. Global Snapshots of the Disturbance Field

Figure 7 shows snapshots of the pressure, density, axial, and radial velocities fluctuations. As pointed out earlier, boundary treatment could cause serious difficulties. The present boundary treatment prevents the generation of spurious waves at the boundaries and proves to be nonreflecting. The wavy nature of the solution apparent in Fig. 7 indicates that the dispersion and dissipation errors of the scheme are negligible. The oscillatory sound source peaks along the jet before it decays downstream. The acoustic waves radiate forward and seem to originate from the streamwise location of the source peak. To validate that the captured disturbance in the outer field is truly acoustics, in Fig. 8 we show a snapshot of the vorticity distribution. The domain shown in Fig. 8 extends $35D$ in the axial direction and $2.5D$ in the radial direction, where the radial coordinate is scaled five times to have a clear view of the vortex structure. Figure 8 shows that the vorticity is concentrated at the shear layer and decays as r increases beyond the shear layer. Thus, waves captured in the domain $r > 2D$ are irrotational, which suggests that they are acoustic waves.

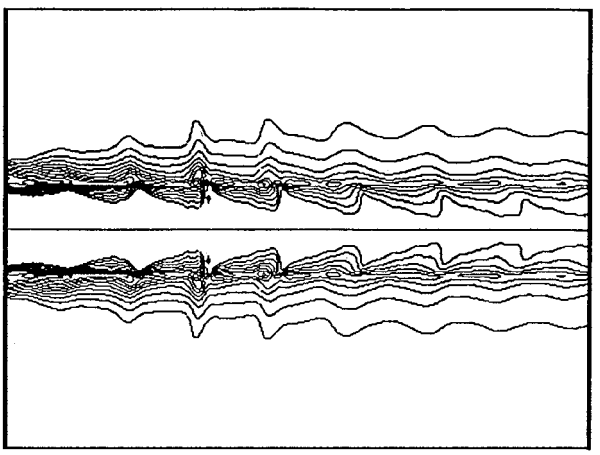

Fig. 8 Instantaneous distribution of vorticity contours at $Sr = 0.2$, $\omega_{min} = 0.0, \omega_{max} = 0.44$, and $\Delta\omega = 0.04$.

C. Acoustic Radiation

Figure 9 shows the rms of the pressure fluctuations for several types of inflow disturbance. For the low initial level case, the flow disturbances continue to grow within the computational domain without forming a peak (Fig. 3). In the corresponding rms of the pressure field, the typically observed lobed shape of the contours is not apparent, which indicates the absence of a peak emission angle. At higher excitation levels, the disturbance peaks within the computational domain, and the lobed shape of the contours is apparent in Figs. 9b and 9c. Thus, the lobed shape of the contours is related to the existence of a streamwise peak of the sound source. For single-frequency excitation, a well-defined peak is apparent. In the bimodal case, two peaks are apparent, each corresponding to a dominant frequency. The emission angle is higher for the higher frequency. In the random disturbance input case, although no dominant Strouhal number at the beginning of the jet, a preferred Strouhal number develops. This corresponds to a peak emission angle, as apparent in Fig. 9d. The shape of the contours, however, is different from that of a single frequency due to the strong nonlinear interactions in the random inflow disturbance case.

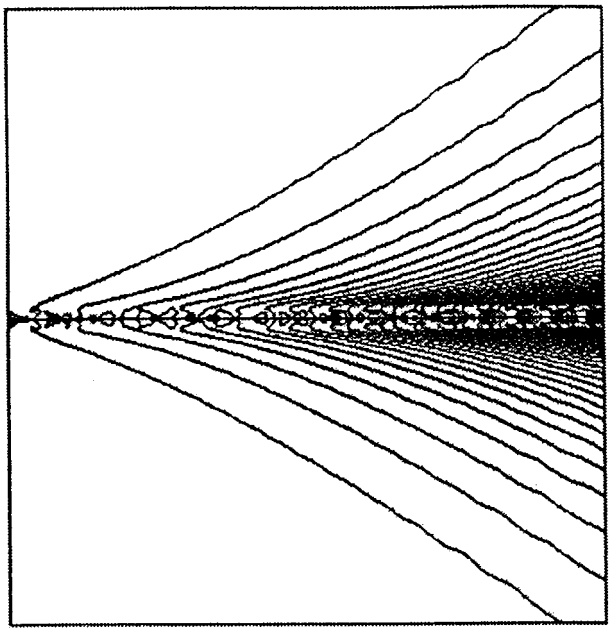

a) Single-frequency excitation, $\epsilon = 0.001$, $p_{\text{rms,min}} = 0$, $p_{\text{rms,max}} = 0.027$, and $\Delta p_{\text{rms}} = 0.0009$

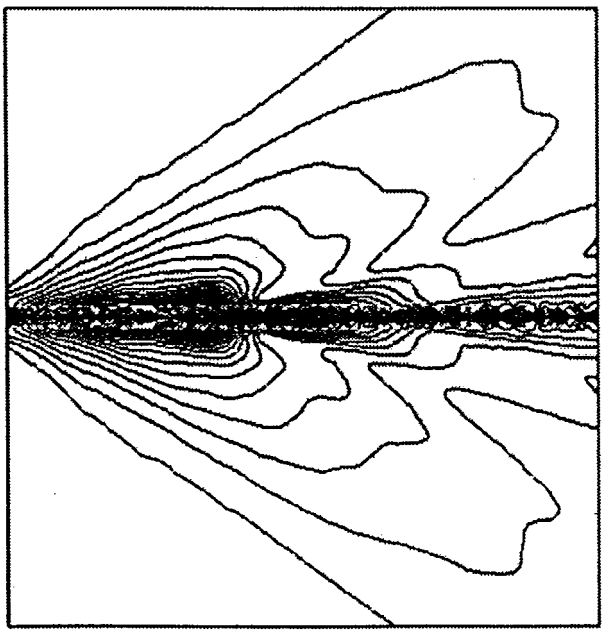

c) Two-frequency excitation, $\epsilon = 0.01$, $p_{\text{rms,min}} = 0$, $p_{\text{rms,max}} = 0.027$, and $\Delta p_{\text{rms}} = 0.0009$

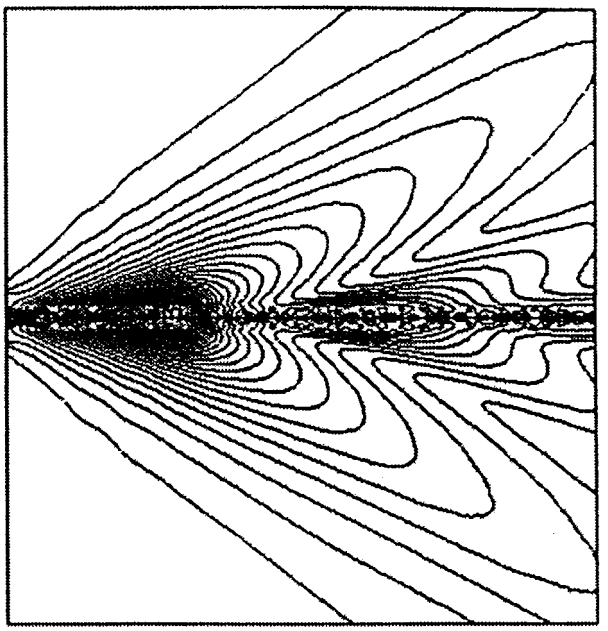

b) Single-frequency excitation, $\epsilon = 0.04$, $p_{\text{rms,min}} = 0$, $p_{\text{rms,max}} = 0.045$, and $\Delta p_{\text{rms}} = 0.00015$

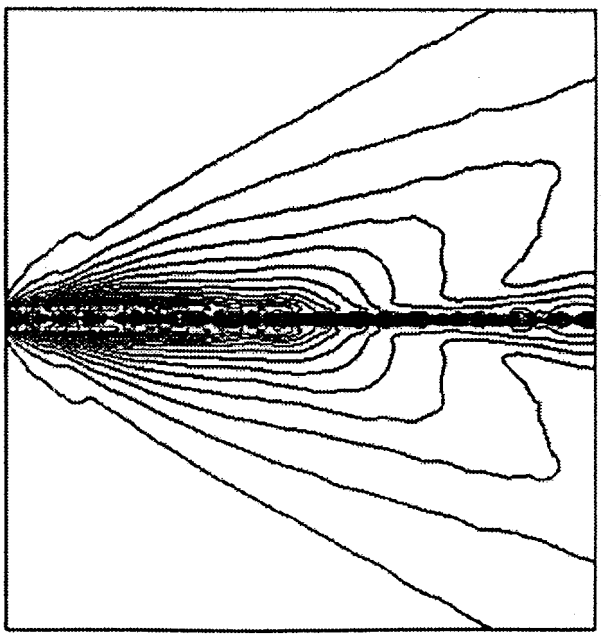

d) Random-frequency excitation, $\epsilon = 0.01$, $p_{\text{rms,min}} = 0$, $p_{\text{rms,max}} = 0.027$, and $\Delta p_{\text{rms}} = 0.0009$

Fig. 9 Pressure fluctuation rms: $p_{\text{rms,min}} = 0$, $p_{\text{rms,max}} = 0.027$, and $\Delta p_{\text{rms}} = 0.0009$.

Troutt and McLaughlin[36] measured the sound field resulting from an $M = 2.1$ jet excited by axisymmetric disturbance at $Sr = 0.2$. However, the measured jet disturbances were found to be dominated by three-dimensional azimuthal modes. The computed sound pressure level (SPL) contours for several inflow disturbances, along with the measurements of Troutt and McLaughlin, are shown in Fig. 10 for comparison purposes. The lobed shapes are the same as in the experiment. We note that the peak of the computed sound depends on the input disturbances.

All computed cases, however, only qualitatively agree with the experiment because the measured peak emission angle is higher than the computed one. The computed disturbances here are limited to two-dimensional axisymmetric ones. In real supersonic jets, the azimuthal modes are more amplified than the axisymmetric modes. The computed spreading rate of the jet is less than the measured one, which influences the peak emission angle. A mean flow with a higher spreading rate would result in better agreement. In the linearized Euler approach,[7] when the proper mean flow is specified, good agreement with the experiment is obtained. Furthermore, the measured directivity and the sound level result from both the axisymmetric and azimuthal modes. The azimuthal modes radiate at higher emission angles compared to the axisymmetric modes, and including their contribution would result in better agreement with the measured peak emission angle.

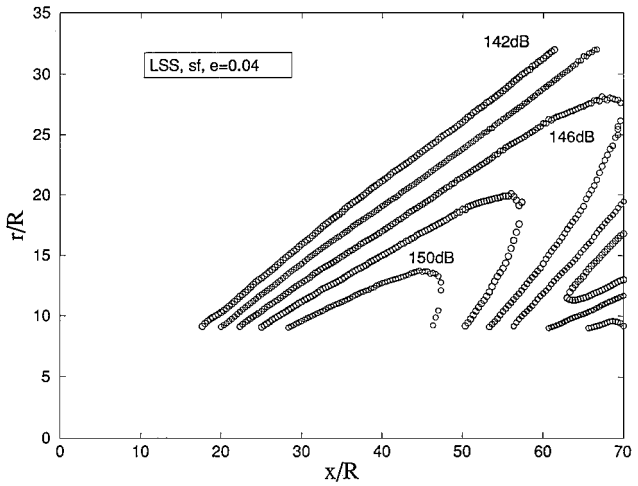

a) Computed, single frequency, $\epsilon = 0.04$

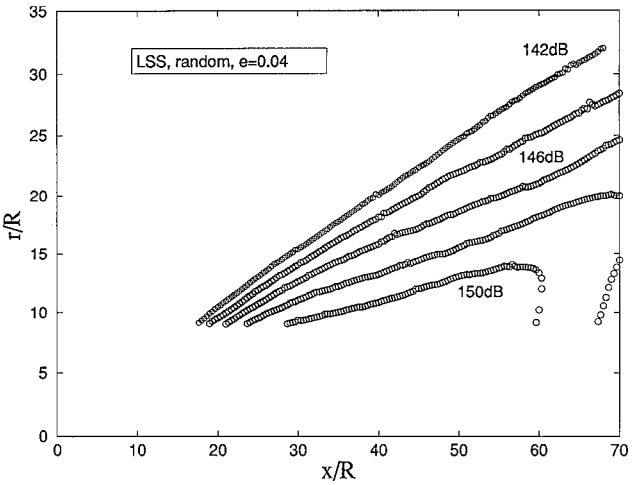

c) Computed, random frequency, $\epsilon = 0.04$

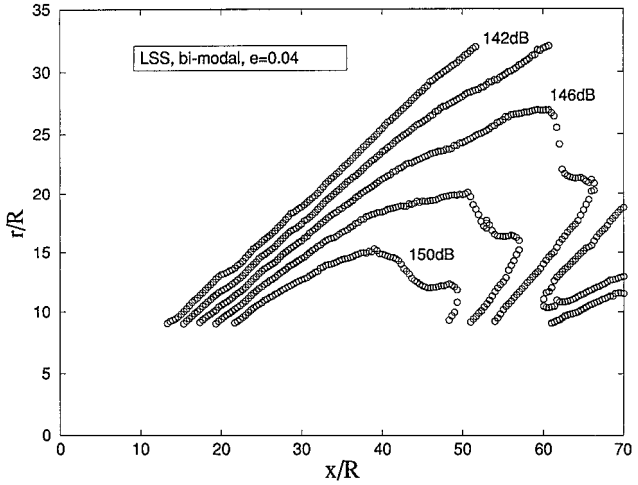

b) Computed, two frequency, $\epsilon = 0.04$

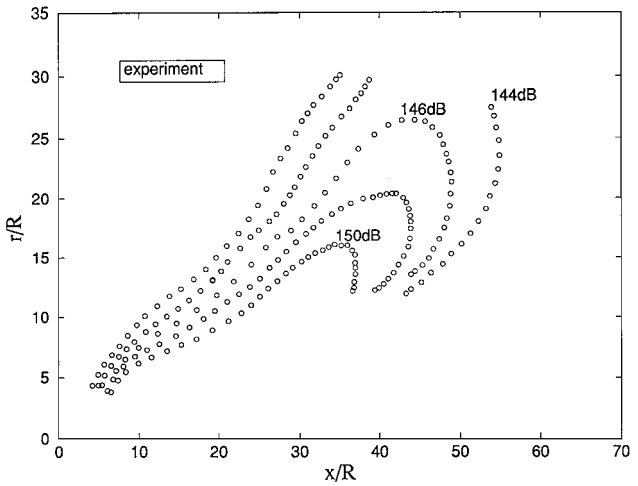

d) Experiment: Troutt and McLaughlin[36]

Fig. 10 SPL contours.

VI. Conclusions

A large-scale simulation capability is developed for direct computation of jet noise. Results are presented for a limited frequency range of the axisymmetric jet structure. The approach, however, could be extended to cover a fully three-dimensional structure and a wider range of scales.

Nonlinear effects on the sound source were found to mimic those of subsonic jets. The initially linear streamwise growth of the disturbances is followed by nonlinear saturation. The location of the peak moves upstream with an increase of the level of inflow disturbances and/or with an increase of the number of inflow modes. Because of nonlinear effects, other modes are generated in addition to the inflow modes. Nonlinear interactions among the various frequency modes control their subsequent development and their radiation field.

Acoustic radiation seems to originate from the streamwise location where the sound source peaks. The looped shape of the rms of the sound pressure contours is associated with the peak of the sound source. The calculated SPLs are in qualitative agreement with observations. However, the computed peak emission angle of the axisymmetric disturbances is lower than the measured one. This suggests that the azimuthal modes radiate at higher angles compared to the axisymmetric ones. The shape of the SPL loops is dependent on the nature of the inflow disturbances, which indicates a potential for controlling jet noise via manipulation of the incoming disturbances.

References

[1]Lesieur, M., and Metais, O., "New Trends in Large Eddy Simulations of Turbulence," *Annual Review of Fluid Mechanics*, Vol. 28, 1996, pp. 45–82.

[2]Liu, C., and Liu, Z. (eds.), "Advances in DNS/LES," *Proceedings of the First AFOSR International Conference on DNS/LES*, Greyden, Columbus, OH, 1997.

[3]Mankbadi, R. R., Hayder, M. E., and Povinelli, L. A., "Structure of Supersonic Jet Flow and Its Radiated Sound," *AIAA Journal*, Vol. 31, No. 5, 1994, pp. 897–906.

[4]Morris, P. J., Wang, Q., Long, L. M., and Lockard, D. P., "Numerical Predictions of High-Speed Jet Noise," AIAA Paper 97-1598, May 1997.

[5]Choi, D., Barber, T. J., Chiappetta, L. M., and Nishimura, M., "Large Eddy Simulation of High-Reynolds Number Jet Flows," AIAA Paper 99-0230, Jan. 1999.

[6]Liu, J. T. C., "Coherent Structures in Transitional and Turbulent Free Shear Flows," *Annual Review of Fluid Mechanics*, Vol. 21, 1989, pp. 285–315.

[7]Mankbadi, R. R., Hixon, D. R., Shih, S.-H., and Povinelli, L. A., "Linearized Euler Equations as a Tool in Jet Noise Prediction," *AIAA Journal*, Vol. 36, No. 2, 1998, pp. 140–147.

[8]Tam, C. K. W., and Burton, D. E., "Sound Generated by Instability Waves of Supersonic Flows. Part 2. Axisymmetric Jets," *Journal of Fluid Mechanics*, Vol. 138, 1984, pp. 273–295.

[9]Dahl, M. D., "Effects of Acoustically Lined Cylindrical Ducts on Instability Waves in Confined Supersonic Jets," AIAA Paper 97-1600, May 1997.

[10]Lighthill, M. J., "On Sound Generated Aerodynamically, Part I, General Theory," *Proceedings of the Royal Society of London, Series A: Mathematical and Physical Sciences*, Vol. 211, 1952, pp. 564–587.

[11]Lyrintzis, A. S., and Mankbadi, R. R., "On the Prediction of the Far-Field Jet Noise Using Kirchhoff's Formulation," *AIAA Journal*, Vol. 34, No. 2, 1996, pp. 413–416.

[12]Mankbadi, R. R., Stuart, T. J, Shih, S.-H., Hixon, D. R., and Povinelli, L. A., "A Surface-Integral Formulation for Jet Noise Prediction that Requires

the Pressure Signal Alone," *Journal of Computational Acoustics*, Vol. 16, No. 3, 1998.

[13]Shih, S.-H., Hixon, D. R., and Mankbadi, R. R., "A Zonal Approach for Prediction of Jet Noise," *Journal of Propulsion and Power*, Vol. 13, No. 6, pp. 745–758.

[14]Tam, C. K. W., "LES for Aeroacoustics," AIAA Paper 98-2805, June 1998.

[15]Mankbadi, R. R., "Review of Computational Aeroacoustics in Propulsion Systems," *Journal of Propulsion and Power*, Vol. 15, No. 3, 1999.

[16]Tam, C. K. W., Golebiowski, M., and Seiner, J. M., "On the Two Components of Turbulent Mixing Noise from Supersonic Jets," AIAA Paper 96-1716, May 1996.

[17]Crighton, D. G., "Acoustics as a Branch of Fluid Mechanics," *Journal of Fluid Mechanics*, Vol. 106, 1981, pp. 261–298.

[18]Liu, J. T. C., "Developing Large-Scale Wavelike Eddies and the Near Jet Noise Field," *Journal of Fluid Mechanics*, Vol. 62, 1974, pp. 437–464.

[19]Tam, C. K. W., and Morris, P. J., "The Radiation of Sound by Instability Waves of a Compressible Plane Turbulent Shear Layer," *Journal of Fluid Mechanics*, Vol. 98, 1980, pp. 349–381.

[20]Seiner, J. M., McLaughlin, D. K., and Liu, C. H., "Supersonic Jet Noise Generated by Large-Scale Instabilities," NASA TP-2072, 1982.

[21]Mankbadi, R. R., *Transition, Turbulence, and Noise*, Kluwer, Dordrecht, The Netherlands, 1994, Chaps. 6, 9.

[22]Smagornisky, J., "General Circulation Experiments with the Primitive Equations. I. The Basic Experiment," *Monthly Weather Review*, Vol. 91, 1963, pp. 99–164.

[23]Edison, T. M., "Numerical Simulation of Turbulent Rayleigh–Bernard Problem Using Numerical Subgrid Modeling," *Journal of Fluid Mechanics*, Vol. 158, 1985, p. 245.

[24]Reynolds, W. C., "The Potential and Limitations of Direct and Large Eddy Simulations, in Whither Turbulence?: Turbulence at the Cross Roads," *Proceedings of the Workshop*, edited by J. L. Lumley, Springer–Verlag, New York, 1989, pp. 245–268.

[25]MacCormack, R. W., "The Effect of Viscosity in Hypervelocity Impact Cratering," AIAA Paper 69-354, 1969.

[26]Gottleib, D., and Turkel, E., "Dissipative Two–Four Methods for Time-Dependent Problems," *Mathematics of Computation*, Vol. 30, April–May 1976, pp. 703–723.

[27]Scott, J. N., Mankbadi, R. R., Hayder, M. E., and Hariharan, S. I., "Outflow Boundary Conditions for the Computational Analysis of Jet Noise," AIAA Paper 93-4366, Oct. 1993.

[28]Tam, C. K. W., "Advances in Numerical Boundary Conditions for Computational Aero-Acoustics," *Journal of Computational Acoustics* (to be published); also AIAA Paper 97-1774, 1997.

[29]Dong, T. Z., and Mankbadi, R. R., "Large-Eddy Simulations of Sound due to Turbulence Inside an Ejector," *Journal of Propulsion and Power*, Vol. 15, No. 3, 1999.

[30]Thompson, K. W., "Time-Dependent Boundary Conditions for Hyperbolic Systems II," *Journal of Computational Physics*, Vol. 89, 1990, pp. 439–461.

[31]Bayliss, A., and Turkel, E., "Far Field Boundary Conditions for Compressible Flows," *Journal of Computational Physics*, Vol. 48, 1982, pp. 182–199.

[32]Hagstrom, T., and Hariharan, S. I., "Far Field Expansion for Anisotropic Wave Equations," *Journal of Computational Acoustics*, Vol. 2, 1990.

[33]Tam, C. K. W., and Webb, J. C., "Dispersion-Relation-Preserving Finite Difference Scheme for Computational Acoustics," *Journal of Computational Physics*, Vol. 107, 1993, pp. 263–281.

[34]Shih, S. H., Hixon, D. R., and Mankbadi, R. R., "Three-Dimensional Structure in a Supersonic Jet: Behavior Near Centerline," *Journal of Computational Fluid Dynamics* (to be published); also AIAA Paper 95-0681, Jan. 1995.

[35]Hixon, D. R., Shih, S.-H., and Mankbadi, R. R., "Treatment of Centerline Singularity in Cylindrical Coordinate System," AIAA Paper 99-2341, 1999.

[36]Troutt, T. R., and McLaughlin, D. K., "Experiments on the Flow and Acoustic Properties of a Moderate-Reynolds-Number Supersonic Jet," *Journal of Fluid Mechanics*, Vol. 116, 1982, pp. 123–156.

[37]Hussain, A. K. M. F., and Zaman, K. B. M. Q., "The Preferred Mode of the Axisymmetric Jet," *Journal of Fluid Mechanics*, Vol. 110, pp. 39–71.